1

SUPPLEMENTARY DATA:

High immunoreactivity of the ^{99m}Tc-F(ab´)2 fragments from in vitro binding studies: After conjugation with HYNIC and labeling with ^{99m}-Technetium, the ^{99m}Tc -F(ab´)2 fragments were purified on PD-10 size-exclusion columns and the radiochemical purity was determined by size-exclusion HPLC equipped with an on-line flow radioactivity detector. The specific activity of the labeled fragments at the time of injection was > 32 mCi/mg. Radiochemical purity greater than 90% was utilized for both in vitro and in vivo imaging studies. Stability analysis in vitro, retention time of the radiolabeled products, and immunoreactivity did not reveal differences between the ^{99m}Tc-F(ab´)$_2$-OKT4A and the ^{99m}Tc -F(ab´)$_2$-CD4R1 radiotracers. The retained specific binding of the ^{99m}Tc -F(ab´)$_2$ products was demonstrated in MT4 cells using a modified method of the saturation cell-binding assay under antigen excess reported by Lindmo and Bunn (1). Binding inhibition with excess amounts of the cold mAb was approximately 99% of the total incubated radioactivity and was independent of the concentration of radiotracer, suggesting that the radioactivity bound to the cell pellet of MT4 cells was the result of specific binding of the radiotracers (Suppl. Fig. S1). The percentage of the labeled fragments bound to cells was > 60% at $4x10^6$ MT4 cells, and its immunoreactivity was estimated to be approximately 100% when extrapolated under condition of excess receptors concentration based on the Lindmo method.

Biodistribution of ^{99m}Tc-F(ab´)2 anti-CD4.
The ^{99m}Tc -F(ab´)$_2$-OKT4A, obtained from the fragmentation of the humanized OKT4A, or the ^{99m}Tc -F(ab´)$_2$-CD4R1, obtained from the fragmentation of the rhesus recombinant CD4R1 which shares the same epitope in D1 domain of OKT4A, were designed with the objective of further reducing immunogenicity observed with the intact monoclonal antibody as assessed *in vivo* in two groups of animals described in Tables S1 and S2. Whole-body and SPECT 3D images were acquired from the top of the skull to the inguinal region for all animals. Figure S2 shows the biodistribution of the two radiolabeled fragments at 4 hrs post injection in two healthy animals. The radiolabeled fragments cleared with a plasma half-life of ~ 10-14 hr, ~ 10-fold faster than the intact radiotracer ^{111}In-DTPA-CDR-OKT4A/huIgG4 previously described (2). The faster clearance of both radiotracers was associated with lower background and overall higher contrast of acquired images compared to the intact monoclonal antibody radiotracer. At visual inspection, similar uptakes of radiotracers were noted in sub-mandibular, axillary and inguinal lymph nodes, the spleen, as well as in the liver. In contrast, lower uptakes of the rhesus recombinant radiotracer compared to the humanized fragment, were observed in the kidneys, suggesting a more favorable biodistribution of the CD4R1 fragment which was established in our program after preliminary imaging studies obtained with the OKT4A fragment. This is consistent with formation of low molecular weight metabolites (of approximately 50 kDa, suggesting formation of Fab) observed in the plasmas of animals injected with the humanized fragment, which accumulate more rapidly in the kidney. This was not observed for the rhesus recombinant fragment. The HPLC analysis of plasma samples collected at 4 hrs following the injection of the radiotracers showed that approximately 90% of the radioactive antibody fragments injected was eluted out with a retention time identical to that of F(ab´)$_2$ for the ^{99m}Tc -F(ab´)$_2$-CD4R1, and to a mixture of F(ab´)$_2$ and F(ab) for the ^{99m}Tc-F(ab´)$_2$-OKT4A (data not shown). All imaging presented in this study were obtained by administering a total mass of the F(ab´)$_2$ tracers of 104.6 ± 21.8 µg. We next examined the effect on the biodistribution of increasing total mass (~ ten fold

higher, ~ 1 mg) of the administered tracers but keeping total radioactivity constant, in 2 uninfected animals with ~1,200 and 350 CD4 PB cell counts, respectively. Both animals showed % of ID in liver or bone marrow (i.e. areas of non specific uptake) approximately half of what we observed in all the other animals that received ~ 100ug. The clearance in the plasma of the tracer was similar, but the peak concentration doubled leading to ~ two fold increase in the area under the curve of the input function. This is consistent with the hypothesis that these compartments act as a saturable sink for the circulating antibody fragment (3). Significant increases in kidney uptakes were also observed in the two uninfected animals. Surprisingly, while the uptakes in the lymph nodes were similar to what was expected from the low mass imaging studies, the spleen was found to be significantly lower (Figure S7).

Specificity of binding in vivo. In order to demonstrate the specificity of radiotracer binding to CD4+ cells *in vivo*, CD4+ cells were isolated from the lymph nodes of two monkeys 6 hours after the administration of the (^{99m}Tc -F(ab´)$_2$-CD4R1)radiotracer and in one monkey 19 hours after the administration of the (^{99m}Tc-F(ab´)$_2$-OKT4A) radiotracer, and the total radioactivity associated with the CD4+ and CD4- cells determined. The levels of the radiotracer associated with the CD4+ cells were consistently higher than the levels of the radiotracer in the CD4- cells (median ratio:~14), similar to our previous observations using the intact radiotracer ^{111}In-DTPA-CDR-OKT4A/huIgG4 (2), thus giving evidence of binding specificity to CD4+ cells *in vivo*.

Immunogenicity analysis.
Plasmas at each imaging time point were screened for immunogenicity and data were excluded from the analyses if animals developed an anti-anti-CD4 immune response. For example, SIVmac251 infected P248 was imaged after baseline (pre-cART) at months 1, 3 and 6 post-cART. Size exclusion (SE)-HPLC (equipped with an on-line flow radioactivity detector) analysis revealed formation of high molecular weight complexes at month 6, consistent with loss of binding to MT4 cells of the radiotracer pre-incubated with plasma at this time point and with a positive ELISA assay against both immobilized antigens (Suppl. Fig. S4). Hence the longitudinal analysis was limited to month 1 and 3 post-cART. H755 did not reveal immunogenic response through the entire period of observation. At month 3 post-cART, the plasma of P261 revealed mild formation of high molecular complexes by SE-HPLC and slight loss of binding by *in vitro* assay, without evidence of antibodies to either the F(ab')$_2$ or the intact OKT4A by ELISA. Sequestration of the radiotracer due to the presence of antibodies in the plasma would underestimate the true uptake in lymphoid tissues. Rhesus P247 and P246 did not reveal immunogenic responses until month 1 and month 5 post-cART, respectively, in any of the three immunogenicity assays.
No evidence of immunogenicity was revealed from either the in vitro MT4 binding assay or SE-HPLC analyses in the plasmas of P773 and P844 until month 3 post-cART. Similarly, no immunogenicity was revealed from either assays in the plasmas of P881 and P731 until month 6 and 3, respectively.

Immunohistochemical staining of fixed tissue of CD3+ cells. Fixed embedded tissues sections were stained with rabbit polyclonal anti-human CD3 antibody (DAKO#A04522, DakoCytomation, Carpenteria, CA, USA). Sections were deparaffinized and rehydrated with four changes of xylene and one change of graded ethanol for 5 min each, followed by

pretreatment for 20 min at 85°C. The samples were sequentially treated with PBS, acqueous hydrogen peroxide, serum block (BSA), the primary anti-CD3 antibody (1:100 dilution) and the secondary antibody biotin conjugated goat anti-rabbit antibody (DAKO#E0432, DakoCytomation, Carpenteria, CA, USA). The reaction was visualized by using AES substrate kit (Vector Laboratories). Samples were then rinsed in distilled water and counterstained with hematoxylin.

Considerations on CD4 receptor occupancy after ^{99m}Tc -F(ab´)$_2$-CD4R1 or the ^{99m}Tc-F(ab´)$_2$-OKT4A administration in nonhuman primates:
Measurements of mean radioactivity per unit cell from the CD4+ and CD4- selections of lymph nodes, were used to extrapolate the receptor occupancy after administration of the radiotracer.

The mean radioactivity level in CD4+ cells extracted from lymph nodes biopsy in a healthy uninfected animal imaged at 19 hrs p.r.i. was 1.52×10^{-2} cpm/cell, after physical ^{99m}Tc decay adjustment to the time of ^{99m}Tc-F(ab´)$_2$-OKT4A injection. Given the specific activity of 7.6 mCi/88 µg at the time of injection, and assuming the mean number of receptors per CD4+ T cells of 80,000 (4), we estimated an occupancy of ~ 1% of CD4 receptors per unit CD4+ cell in the lymph nodes. Measurements of cpm/g in spleen and lymph nodes at earlier time points, suggest that the occupancy in the spleen is ~ 2-3 fold higher compared to the lymph nodes. Radiotracer uptake levels, in a second healthy animal necropsied at 21 hrs post ^{99m}Tc-F(ab´)$_2$-CD4R1 injection, were ~10^8 [cpm/g] and ~0.5×10^8 [cpm/g] for the spleen and mean lymph nodes, respectively (adjusted to the time of radiotracer injection). Given the specific activity of 7.5 mCi/96 µg at the time of injection and assuming ~10^9 CD4+ cells per gram (5), we estimated an occupancy of ~ 5% of CD4 receptors per unit CD4+ cell in the spleen (and ~ half in the lymph nodes). The latter requires also to assume that the majority of the uptake in these organs is specific, (as supported by the range of radiotracer uptakes observed between healthy and immune-depleted hosts in the same organs). The higher occupancy in the spleen is expected because of the higher blood flow in this organ compared to the lymph nodes, and higher uptakes in the spleen are also expected during the earlier hours of the biodistribution (from dynamics analyses, not shown). We have not produced ex-vivo data to provide a similar estimate of max occupancy in the spleen or lymph nodes when the monkeys are injected with ~ ten-fold higher mass of this probe (~ 1 mg).

Considerations on total mass of the anti-CD4 probe administration:
In our study we injected a total mass ~ 100 µg of the ^{99m}Tc -F(ab´)$_2$-CD4R1 (~ 5 mCi total radioactivity), which is ten fold lower the mass injected of the ^{64}Cu -F(ab´)$_2$-CD4R1 described in Byrareddy et al (6), and more recently in (7) . To further examine the effect of the total mass injected of the probe on the relative uptake in vivo, we administered ~ 1 mg of the probe keeping constant the radioactivity dose (~ 5 mCi total radioactivity) in 3 healthy uninfected animals (Table S3) and imaged them at 19 hrs p.r.i. along with a group of 4 healthy animals administered ~100ug. The MTM and MZC animals belonging to the high and low dose groups, respectively, were sacrificed and tissues harvested for gamma counter measurements of probe uptake ex-vivo

and planar imaging (similar to the ex-vivo analysis described in Figure 6 for animals imaged with the 100 μg dose).

By increasing of ~ ten-fold the total mass of tracer injected (from ~ 100 μg to ~ 1 mg), we observed from the imaging analyses, an increased uptake in the kidney, and decrease of uptake in the liver, bone marrow as well as a dramatic decrease in the spleen (to reach levels similar to those reported in (6, 7)) and to a lower extent, in the lymph nodes, hence providing some evidence of saturability of these lymphoid compartments when 1 mg mass of the probe is administered (3) (Suppl Fig. S7). We also observed an increased uptake in the plasma (~2 fold higher AUC_{0-19hr} in the 1 mg biodistribution compared to the 100 μg dose).

Ex-vivo data showed that the relative anti-CD4 probe uptake in the intestinal walls remains low compared to the spleen also when the dose of the probe is increased of ten fold (Suppl Fig S8 and S9).

Despite these similarities between the biodistribution of the ^{99m}Tc -F(ab´)$_2$-CD4R1 and some aspects of the ^{64}Cu -F(ab´)$_2$-CD4R1 biodistribution generated from in vivo imaging analyses as reported in (8), when both tracers are injected at 1 mg dose, we were not able to see similar high uptakes in the gut. The authors reported in their studies, similar uptakes of the probe in the gut and lymph nodes of healthy animals. Hence, since detailed PK kinetic studies, to exclude differential probe penetration in these compartments, are difficult due to the low mass of the probe injected, we have further radiolabeled the Fab'2-CD4R1 with ^{64}Cu (conjugated with DOTA) and studied its biodistribution in one healthy animal. The SUV levels shown in Suppl Fig S9 suggest high similarity between the two tracers, with a non visible evidence of higher penetration of the ^{64}Cu probe in the intestines compared to the ^{99m}Tc probe. While the max ^{64}Cu -F(ab´)$_2$-CD4R1 uptake in the gut harvested on a tray (Suppl Fig S9) reaches levels similar to LNs (as also observed with the ^{99m}Tc -F(ab´)$_2$-CD4R1 tracer), the mean uptake was found to be approx. ten fold lower than the max uptake, hence revealing the high heterogeneity of the CD4 probe uptake biodistribution in the gut

Two additional groups of two animals each, were euthanized at 6 hr and 21 hr, respectively, following ^{99m}Tc-F(ab´)$_2$-CD4R1 imaging (using ~100 microgram total mass). Large sections of the jejunum and colon, as well as other organs were harvested, placed on a tray and imaged with the SPECT camera. Small aliquots of these organs were also counted with the gamma counter. Each group consisted of one healthy and one SIV infected animal with high and low PB CD4+ T cell count, respectively. The SIV infected animal necropsied at 21 hr post radiotracer injection, was also administered a highly selective anti-CD3 immunotoxin to further deplete the CD4 pool in tissues (9), one week prior to the necropsy study. Both animals in the 21hr group also underwent axillary and rectal mucosal biopsies at 3 hr p.r.iFollowing radiotracer injection, the input functions were generated for both animals imaged up to 21 hr p.r.i. and then necropsied.

Suppl. Fig S5 and Figure 6 show the organs placed on the trays, harvested from necropsies conducted at 6 and 21 hr p.r.i, respectively.
Figure 6.A shows the entire jejunum and entire ileum (>95% of the small intestines) laid on a tray with a portion of the mesentery (~50% of the entire mesentery in the body) attached to the intestine walls. The mesentery is a double fold of peritoneum, fan-shaped which covers the entire

length of the jejunum and ileum. Between the 2 leaves of the mesentery are the mesenteric vessels, fat and mesenteric lymph nodes.

As shown from the planar images of the trays (Figure 6B), isolated discrete areas of high radiotracer uptakes can be seen in both the healthy and infected animals, with few of these discrete spots reaching levels similar to the uptake in the LNs. Of note, in the healthy animal, we identified only 4 hot areas, with 3 of them localizing in the mesentery compartment, but not in the intestines. Consistent with the ex-vivo measurements obtained with the 1 mg mass of the probe, only lymphnodes and spleen show lower uptake of the probe in the CD4 depleted animals, however the vast majority of the areas in the intestinal walls show radiotracer uptakes similar between the healthy and the CD4 depleted animals. Moreover, the mean SUV of the intestines was stable (~1) comparing the 6 hr (Fig. S5) and 21 hr p.r.i. (Fig. 6) ex-vivo biodistributions. We believe that the above biodistribution of the anti-CD4 probe is consistent with the differential concentration of CD4 T cells in those anatomic compartments. Figure S6 (previously published by our team (5)) shows at two different magnifications the distribution of CD3+ cells in tissue sections of small, large intestines as well as in lymph nodes and spleen. As can be seen from visual inspection, the CD3+ concentration per unit area of tissue is much higher in the lymph nodes and spleen, where the majority of mononuclear cells are lymphocytes which occupy most of the area. Conversely, in the small and large intestines, the majority of the area is occupied by the muscularis externa and submucosa compartments, which harbor a negligible amount of lymphocytes in between fat layers.

References

1.   Lindmo T, and Bunn PA, Jr. Determination of the true immunoreactive fraction of monoclonal antibodies after radiolabeling. *Methods Enzymol.* 1986;121:678-91.
2.   Di Mascio M, Srinivasula S, Bhattacharjee A, Cheng L, Martiniova L, Herscovitch P, et al. Antiretroviral tissue kinetics: in vivo imaging using positron emission tomography. *Antimicrob Agents Chemother.* 2009;53(10):4086-95.
3.   Pandit-Taskar N, O'Donoghue JA, Morris MJ, Wills EA, Schwartz LH, Gonen M, et al. Antibody mass escalation study in patients with castration-resistant prostate cancer using 111In-J591: lesion detectability and dosimetric projections for 90Y radioimmunotherapy. *J Nucl Med.* 2008;49(7):1066-74.
4.   Zamarchi R, Panozzo M, Del Mistro A, Barelli A, Borri A, Amadori A, et al. B and T cell function parameters during zidovudine treatment of human immunodeficiency virus-infected patients. *J Infect Dis.* 1994;170(5):1148-56.
5.   Di Mascio M, Paik CH, Carrasquillo JA, Maeng JS, Jang BS, Shin IS, et al. Noninvasive in vivo imaging of CD4 cells in simian-human immunodeficiency virus (SHIV)-infected nonhuman primates. *Blood.* 2009;114(2):328-37.
6.   Byrareddy SN, Arthos J, Cicala C, Villinger F, Ortiz KT, Little D, et al. Sustained virologic control in SIV+ macaques after antiretroviral and alpha4beta7 antibody therapy. *Science.* 2016;354(6309):197-202.
7.   Santangelo PJ, Cicala C, Byrareddy SN, Ortiz KT, Little D, Lindsay KE, et al. Early treatment of SIV+ macaques with an alpha4beta7 mAb alters virus distribution and preserves CD4(+) T cells in later stages of infection. *Mucosal Immunol.* 2017.
8.   Sanders-Beer BE, Voronin Y, McDonald D, and Singh A. Harnessing Novel Imaging Approaches to Guide HIV Prevention and Cure Discoveries-A National Institutes of

       Health and Global HIV Vaccine Enterprise 2017 Meeting Report. *AIDS Res Hum Retroviruses.* 2018;34(1):12-26.

9.   Matar AJ, Pathiraja V, Wang Z, Duran-Struuck R, Gusha A, Crepeau R, et al. Effect of pre-existing anti-diphtheria toxin antibodies on T cell depletion levels following diphtheria toxin-based recombinant anti-monkey CD3 immunotoxin treatment. *Transpl Immunol.* 2012;27(1):52-4.

Supplementary FIGURE LEGENDS

Supp. Figure S1. *In vitro* cell binding assay. Total binding (duplicates; red and blue) and non-specific binding (black) of ^{99m}Tc -F(ab´)$_2$-OKT4A (**A**) or ^{99m}Tc -F(ab´)$_2$-CD4R1 (**B**) to CD4 receptor was tested using MT4 cells.

Supp. Figure S2. MIP -images of healthy monkeys. Maximum Intensity Projection (MIP)-SPECT images in the skull, abdominal and pelvic field of view (FOV) in two healthy monkeys imaged at 4 hrs post injection with ^{99m}Tc-F(ab´)$_2$-OKT4A or ^{99m}Tc-F(ab´)$_2$-CD4R1, respectively. Tissue uptakes were converted to RAINBOW color scale as shown in color bar, where red color indicates highest retention. Differing contrasts in the fields of views (FOVs) were applied to highlight lymph nodes and spleen. Arrows point to specific tissues of interest along with imaging standard. While similar uptake was observed in lymphoid tissues, a differential uptake was observed in kidneys consistent with the detection of formation of Fab from ^{99m}Tc-F(ab´)$_2$-OKT4A in the plasma which accumulated in the kidneys.

Supp. Figure S3. Relationship between CD4+ T cell counts in the peripheral blood and radiotracer retention (top panels) or SUVmax (bottom panels), estimated from SPECT images. All animals were categorized into 6 groups based on peripheral CD4+ T cell counts. Black dots shows the mean retention within each group and error bars are 1*Std. Error of the mean.

Supp. Figure S4. Immune Response to the Radiotracer. Formation of high molecular weight immune complexes in plasma can be detected by HPLC as early as 3-4 weeks following incubation with the radiotracer. Radiochromatograms were transformed into probability density curves by normalizing for the area under the curve. HPLC chromatograms are in parallel with the plasma binding assay and ELISA results (shown as an insert in each HPLC histogram). As a negative control, plasma from an unexposed monkey (black dash) was run through HPLC on the same day in addition to gel-filtration HPLC standard mixture (as shown in first panel) containing 5 standard components with different molecular weights (MW) (bovine thyroglobulin (MW 670,000 Daltons (D); brown), bovine ɤ-globulin (MW 158,000D; green), chicken ovalbumin (MW 44,000D; blue), horse myoglobin (MW 17,000D; purple), and vitamin B12 (MW 1,350D; black)). In the depicted example the host became immunogenic after the 3rd imaging.

Supp. Figure S5. . One healthy (A) and one SIV infected (B) animal were necropsied at 6 hr p.r.i. following imaging. The entire jejunum and entire ileum (>95% of the small intestines) and entire colon laid on a tray with a portion of the mesentery (~50% of the entire mesentery) attached to the intestine walls. Tissue uptakes normalized on plasma levels were converted to RAINBOW color scale as shown in color bar, where red color indicates highest uptake.

Supp. Figure S6. Immunohistochemical staining of fixed tissue of CD3+ cells. a, Uninfected tissue sections of colon, jejunum, spleen, axillary and sub-mandibular lymph nodes; top panels: sections were acquired at magnification x50. bottom panels: sections were acquired at magnification x200

Supp. Figure S7. Effect of mass on biodistribution of the ^{99m}Tc-F(ab´)$_2$-CD4R1 (in vivo imaging). SUV of plasma, and SUVmax of axillary and sub-mandibular lymph nodes, heart, bone marrow, spleen, kidney and liver of animals imaged at 19 hrs post radiotracer injection, with ~100 µg (red dots) or ~1 mg (blue dots).

Supp. Figure S8. Effect of mass on biodistribution of the ^{99m}Tc-F(ab´)$_2$-CD4R1 (ex-vivo imaging). Two healthy animals were administered ~100 µg (A) and ~1 mg (B) of the ^{99m}Tc-F(ab´)$_2$-CD4R1 and necropsied at 21hr p.r.i. The entire jejunum and entire ileum (>95% of the small intestines) laid on a tray with a portion of the mesentery (~50% of the entire mesentery) attached to the intestine walls and a portion of the colon, were imaged before and after removal of the feces. The feces account for ~15% of the total radioactivity in the small and large intestines. Tissue uptakes were converted to a RAINBOW color scale, where red color indicates highest uptake. Pre and post-feces removal images were adjusted within each animal. Yellow circles separate small and large intestines.

Supp. Figure S9. Effect of mass on biodistribution of the ^{64}Cu-F(ab´)$_2$-CD4R1 (ex-vivo imaging). One healthy animals was administered ~1,000 µg of the ^{64}Cu-F(ab´)$_2$-CD4R1 and necropsied at 18 hr p.r.i. At necropsy, organs were harvested and counted in gamma counter for SUV determination (A). The entire jejunum and entire ileum (>95% of the small intestines, outside the yellow circle) and entire colon (inside the yellow circle) laid on a tray, were imaged after removal of the feces. (B). Tissue uptakes were converted to a RAINBOW color scale, where red color indicates highest uptake.

Supplementary Figures and Tables

Table S1A-B

Animal ID	Gender	Age (y)	Weight (kg)	SIV strain	Duration of infection, Weeks	CD4+ T cells/µl	CD8+ T cells/µl	CD20+ B cells/µl	Log (SIV-RNA) copies/ml	Tc99m inj. dose, mCi
A5E036	Male	5.8	8.55	SIV-tk	42	1324	464	441	1.95	6.97
CE7E	Female	13.8	6.25	Uninfected	N/A	1267	1103	308	N/A	4.01
01D278	Female	10.5	5.45	Uninfected	N/A	922	753	603	N/A	8.23
CF67	Male	10.9	10.00	Uninfected	N/A	755	663	296	N/A	5.28
XAW	Male	13.7	7.25	Uninfected	N/A	734	591	395	N/A	7.38
DBPN	Male	6.2	11.80	Uninfected	N/A	699	507	532	N/A	5.88
P246	Female	5.8	6.20	SIV-mac251	28	295	252	407	5.73	6.22
H755	Male	9.6	9.95	SIVE543	72	121	555	356	6.84	4.51
P261	Female	5.0	6.90	SIV-mac251	27	86	156	531	6.57	5.76
P248	Female	5.6	5.40	SIV-mac251	27	68	321	101	6.25	6.94
P247	Female	5.8	5.70	SIV-mac251	28	28	183	342	5.66	5.28

Animal ID	Gender	Age (y)	Weight (kg)	SIV strain	Duration of infection, Weeks	CD4+ T cells/µl	CD8+ T cells/µl	CD20+ B cells/µl	Log (SIV-RNA) copies/ml	Tc99m inj. dose, mCi
P707	MALE	10.2	9.9	SIVmac251	117	1718	2227	1017	3.86	6.20
DCDK	MALE	5.3	7.3	Uninfected	NA	1506	1107	841	N/A	6.35
P881	MALE	6.6	10	SIVmac251	123	1475	1492	544	0.85	6.09
A5E006	MALE	7.1	11.85	SIV-tk	99	1281	1587	374	< 1.48	5.77
DCAK	MALE	5.3	7.9	Uninfected	NA	1275	1004	1131	N/A	5.35
DCBP	MALE	6.5	11.95	SIVmac239	23	1076	1254	1433	3.61	4.83
DBIJ	MALE	8.4	9.4	Uninfected	NA	1054	890	434	N/A	7.85
H572	MALE	15.5	8.7	Uninfected	NA	951	654	278	N/A	9.04
P887	MALE	6.7	11.4	SIVmac251	123	836	797	296	1.18	4.34
DCKJ	MALE	5.1	6.95	Uninfected	NA	730	535	605	N/A	5.54
ZD21	FEMALE	10.5	5.95	Uninfected	NA	691	421	363	N/A	5.23
P868	MALE	7.3	12.45	SIVmac251	99	685	685	1588	1.30	6.72
P844	FEMALE	7.1	10.3	SIVmac251	113	494	1523	1411	3.46	5.13
DCET	MALE	5.1	7	Uninfected	NA	437	390	496	N/A	6.40
P731	MALE	11.1	8.2	SIVmac251	152	355	462	180	0.30	6.67
P773	FEMALE	6.7	8.85	SIVmac251	113	215	324	402	6.18	6.74
P636	MALE	7.2	8.05	SIVmac251	33	198	385	673	6.04	6.77
DA24	MALE	9.9	9.15	SHIVAD8	149	83	180	214	4.59	5.54
G43	FEMALE	6.7	5.45	SHIVDH12R\SIVmac239	87	7	338	215	5.15	5.77

Supplementary Table S2A

Animal ID	Camera	Tracer	Tc99m inj. dose (mCi)	Specific Activity (μCi/μg)
A5E036	Triad, Trionix	^{99m}Tc -F(ab´)$_2$-OKT4A	6.97	63.4
CE7E	Symbia T2, Siemens	^{99m}Tc -F(ab´)$_2$-OKT4A	4.01	31.9
01D278	Symbia T2, Siemens	^{99m}Tc -F(ab´)$_2$-OKT4A	8.23	78.6
CF67	Triad, Trionix	^{99m}Tc -F(ab´)$_2$-OKT4A	5.28	42.9
XAW	Symbia T2, Siemens	^{99m}Tc -F(ab´)$_2$-OKT4A	7.38	71.0
DBPN	Triad, Trionix	^{99m}Tc -F(ab´)$_2$-OKT4A	5.88	41.7
P246 - 1st Baseline	Triad, Trionix	^{99m}Tc -F(ab´)$_2$-OKT4A	6.22	79.7
P246 - 2nd Baseline	Triad, Trionix	^{99m}Tc -F(ab´)$_2$-OKT4A	7.55	55.7
P246 - 3rd Baseline	Symbia T2, Siemens	^{99m}Tc -F(ab´)$_2$-OKT4A	5.38	60.2
P246 -Month (1)	Symbia T2, Siemens	^{99m}Tc -F(ab´)$_2$-OKT4A	5.98	91.7
P246 - Month (3)	Symbia T2, Siemens	^{99m}Tc -F(ab´)$_2$-CD4R1	6.03	51.5
P246 - Month (5)	Symbia T2, Siemens	^{99m}Tc -F(ab´)$_2$-CD4R1	6.29	54.5
H755 - 1st Baseline	Triad, Trionix	^{99m}Tc -F(ab´)$_2$-OKT4A	4.51	41.1
H755 - 2nd Baseline	Triad, Trionix	^{99m}Tc -F(ab´)$_2$-OKT4A	5.28	45.7
H755 - Month (1)	Triad, Trionix	^{99m}Tc -F(ab´)$_2$-OKT4A	5.58	53.3
H755 - Month (3)	Triad, Trionix	^{99m}Tc -F(ab´)$_2$-OKT4A	7.44	56.4
H755 - Month (5)	Triad, Trionix	^{99m}Tc -F(ab´)$_2$-OKT4A	6.66	49.0
H755 - Month (9)	Symbia T2, Siemens	^{99m}Tc -F(ab´)$_2$-OKT4A	7.10	65.9
H755 - Month (12)	Symbia T2, Siemens	^{99m}Tc -F(ab´)$_2$-OKT4A	6.29	78.1
H755 - Month (14)	Symbia T2, Siemens	^{99m}Tc -F(ab´)$_2$-CD4R1	7.14	63.1
H755 - Month (19)	Symbia T2, Siemens	^{99m}Tc -F(ab´)$_2$-CD4R1	4.76	74.6
P261 - Baseline	Triad, Trionix	^{99m}Tc -F(ab´)$_2$-OKT4A	5.76	41.0
P261 - Month (1)	Triad, Trionix	^{99m}Tc -F(ab´)$_2$-OKT4A	5.13	36.2
P261 - Month (3)	Triad, Trionix	^{99m}Tc -F(ab´)$_2$-OKT4A	6.09	43.0
P248 - Baseline	Triad, Trionix	^{99m}Tc -F(ab´)$_2$-OKT4A	6.94	48.5
P248 - Month (1)	Triad, Trionix	^{99m}Tc -F(ab´)$_2$-OKT4A	6.49	47.8
P248 - Month (3)	Triad, Trionix	^{99m}Tc -F(ab´)$_2$-OKT4A	6.88	66.1
P247 - Baseline	Triad, Trionix	^{99m}Tc -F(ab´)$_2$-OKT4A	5.28	36.2
P247 - Month (1)	Triad, Trionix	^{99m}Tc -F(ab´)$_2$-OKT4A	6.49	47.5

Supplementary Table S2B

Animal ID	Camera	Tracer	Tc99m inj. dose (mCi)	Specific Activity (µCi/µg)
P707	Symbia T2, Siemens	^{99m}Tc -F(ab')$_2$-CD4R1	6.20	76.7
DCDK	Symbia T2, Siemens	^{99m}Tc -F(ab')$_2$-CD4R1	6.35	73.6
P881 - Baseline	Symbia T2, Siemens	^{99m}Tc -F(ab')$_2$-CD4R1	6.09	70.5
P881 - Month (1)	Symbia T2, Siemens	^{99m}Tc -F(ab')$_2$-CD4R1	6.80	92.2
P881 - Month (3)	Symbia T2, Siemens	^{99m}Tc -F(ab')$_2$-CD4R1	5.42	53.9
P881 - Month (7)	Symbia T2, Siemens	^{99m}Tc -F(ab')$_2$-CD4R1	6.91	99.4
A5E006	Symbia T2, Siemens	^{99m}Tc -F(ab')$_2$-CD4R1	5.77	43.3
DCAK	Symbia T2, Siemens	^{99m}Tc -F(ab')$_2$-CD4R1	5.35	60.4
DCBP	Symbia T2, Siemens	^{99m}Tc -F(ab')$_2$-CD4R1	4.83	63.1
DBIJ	Symbia T2, Siemens	^{99m}Tc -F(ab')$_2$-CD4R1	7.85	65.5
H572	Symbia T2, Siemens	^{99m}Tc -F(ab')$_2$-CD4R1	9.04	90.6
P887	Symbia T2, Siemens	^{99m}Tc -F(ab')$_2$-CD4R1	4.34	52.2
DCKJ	Symbia T2, Siemens	^{99m}Tc -F(ab')$_2$-CD4R1	5.54	63.5
ZD21	Symbia T2, Siemens	^{99m}Tc -F(ab')$_2$-CD4R1	5.23	53.3
P868	Symbia T2, Siemens	^{99m}Tc -F(ab')$_2$-CD4R1	6.72	76.5
P844 - 1st Baseline	Symbia T2, Siemens	^{99m}Tc -F(ab')$_2$-CD4R1	5.13	57.4
P844 - 2nd Baseline	Symbia T2, Siemens	^{99m}Tc -F(ab')$_2$-CD4R1	5.12	51.5
P844 - Month (1)	Symbia T2, Siemens	^{99m}Tc -F(ab')$_2$-CD4R1	6.37	66.7
P844 - Month (3)	Symbia T2, Siemens	^{99m}Tc -F(ab')$_2$-CD4R1	6.60	66.6
DCET	Symbia T2, Siemens	^{99m}Tc -F(ab')$_2$-CD4R1	6.40	77.9
P731 - Baseline	Symbia T2, Siemens	^{99m}Tc -F(ab')$_2$-CD4R1	6.67	65.5
P731 - Month (1)	Symbia T2, Siemens	^{99m}Tc -F(ab')$_2$-CD4R1	6.44	71.1
P731 - Month (3)	Symbia T2, Siemens	^{99m}Tc -F(ab')$_2$-CD4R1	6.22	59.5
P773 - 1st Baseline	Symbia T2, Siemens	^{99m}Tc -F(ab')$_2$-CD4R1	6.74	71.0
P773 - 2nd Baseline	Symbia T2, Siemens	^{99m}Tc -F(ab')$_2$-CD4R1	6.55	68.2
P773 - Month (1)	Symbia T2, Siemens	^{99m}Tc -F(ab')$_2$-CD4R1	5.37	54.3
P773 - Month (3)	Symbia T2, Siemens	^{99m}Tc -F(ab')$_2$-CD4R1	5.29	54.6
P636	Symbia T2, Siemens	^{99m}Tc -F(ab')$_2$-CD4R1	6.77	67.4
DA24	Symbia T2, Siemens	^{99m}Tc -F(ab')$_2$-CD4R1	5.54	54.7
G43	Symbia T2, Siemens	^{99m}Tc -F(ab')$_2$-CD4R1	5.77	67.0

Suppl. Figure S1

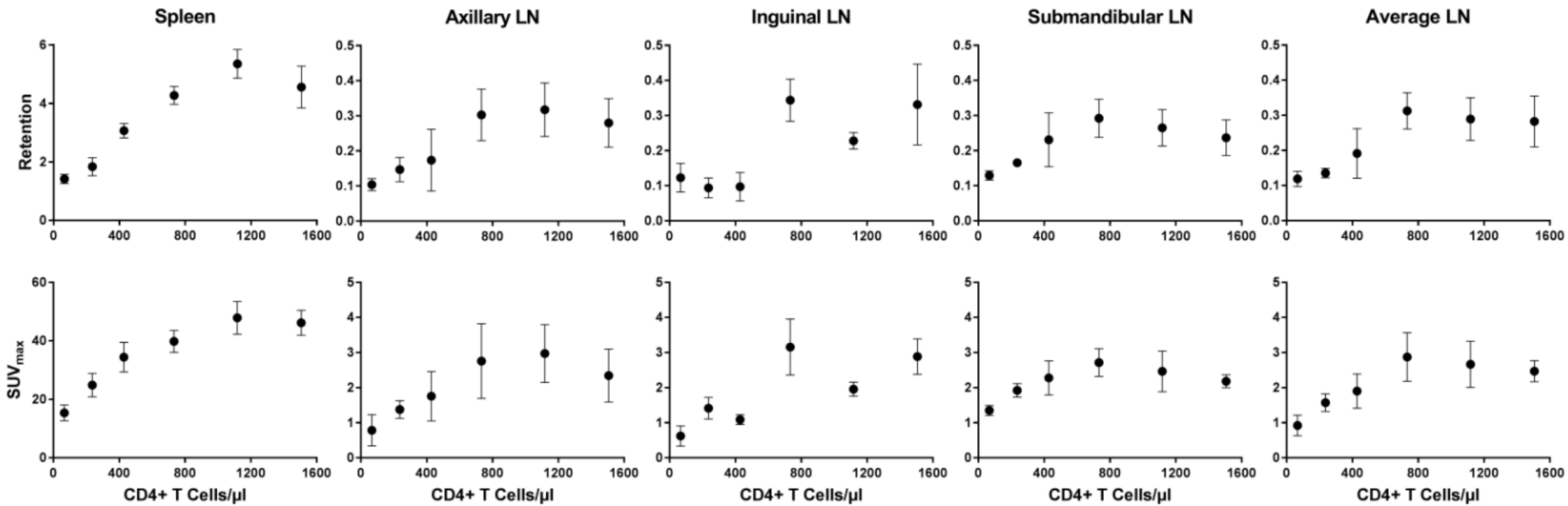Cell binding assay: hot (duplicates) and cold-competition
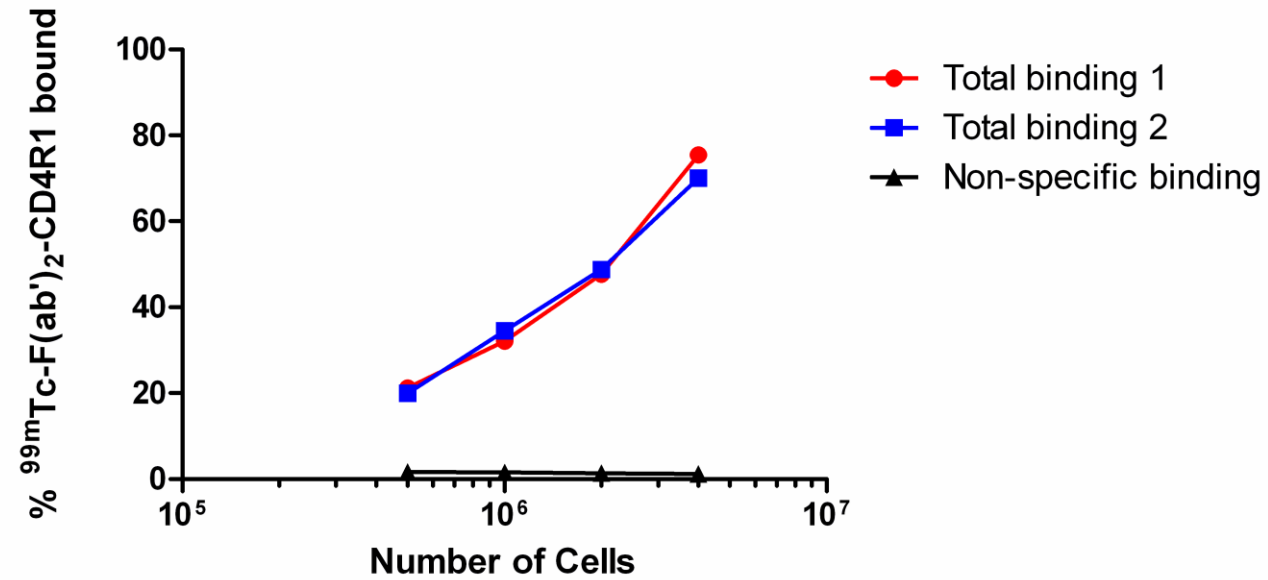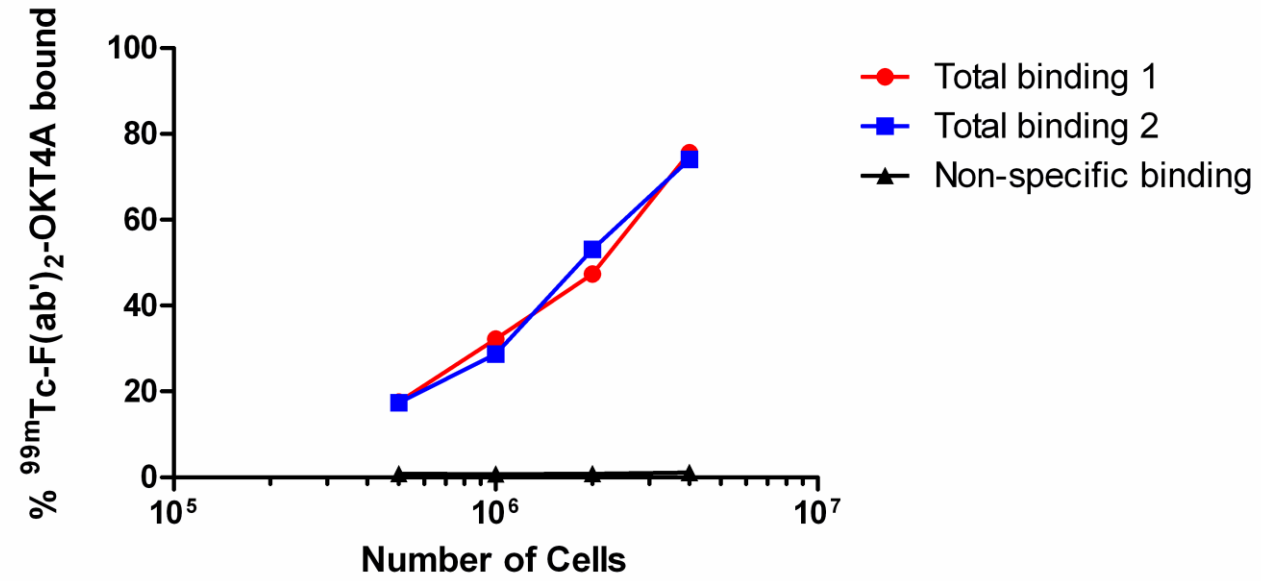
Suppl. Figure S2

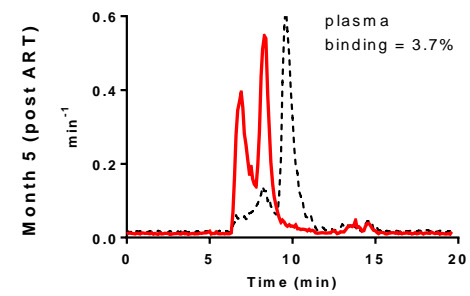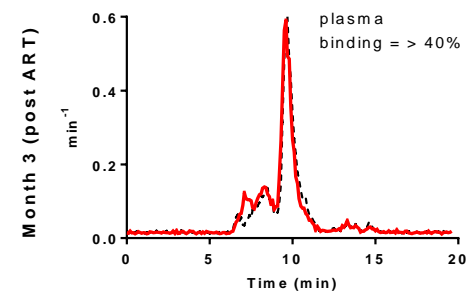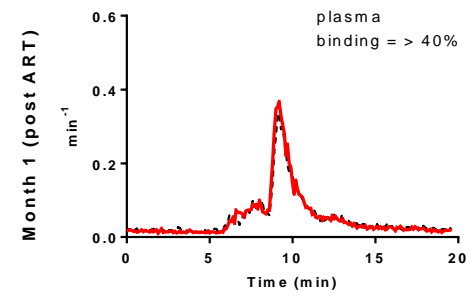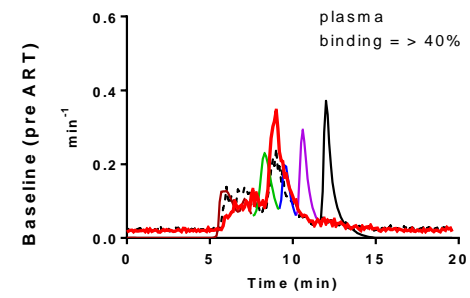**Biodistribution of humanized and rhesus-recombinant F(ab')2 anti-CD4**
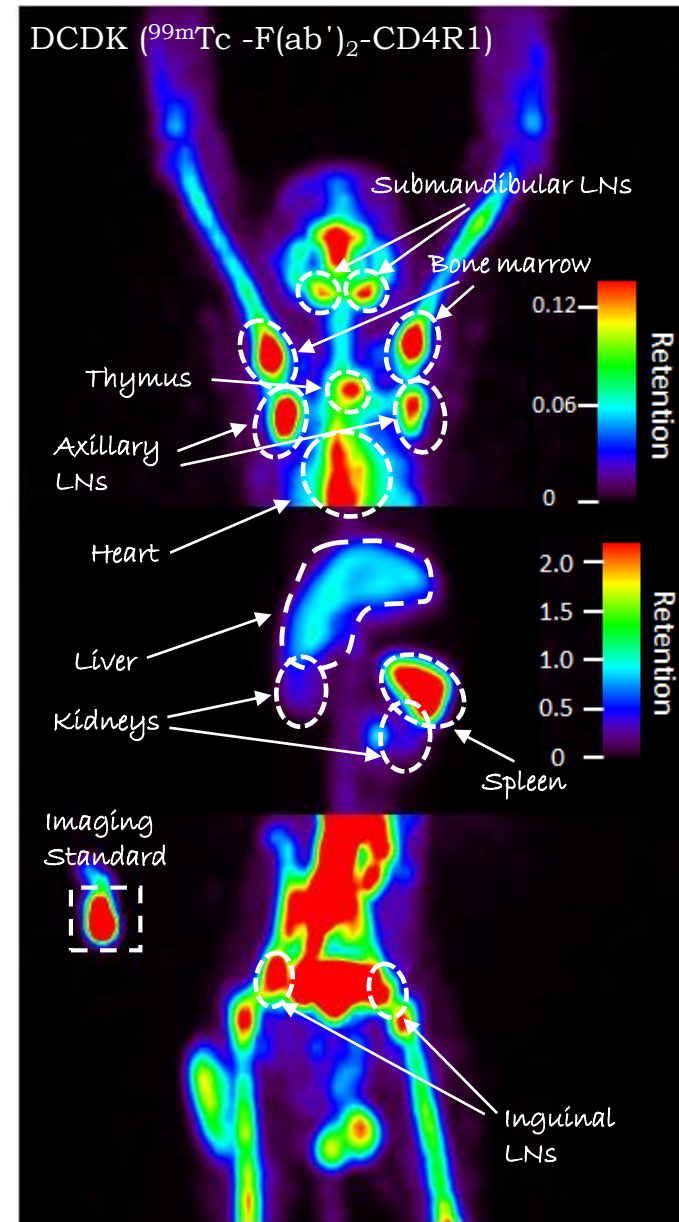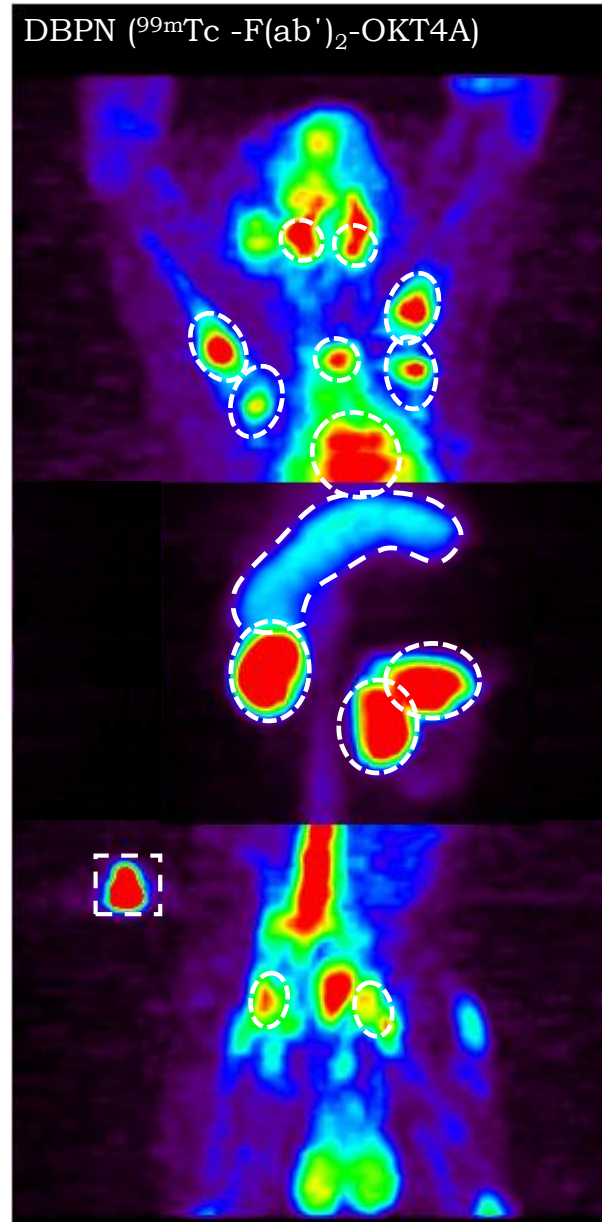
Suppl. Figure S3

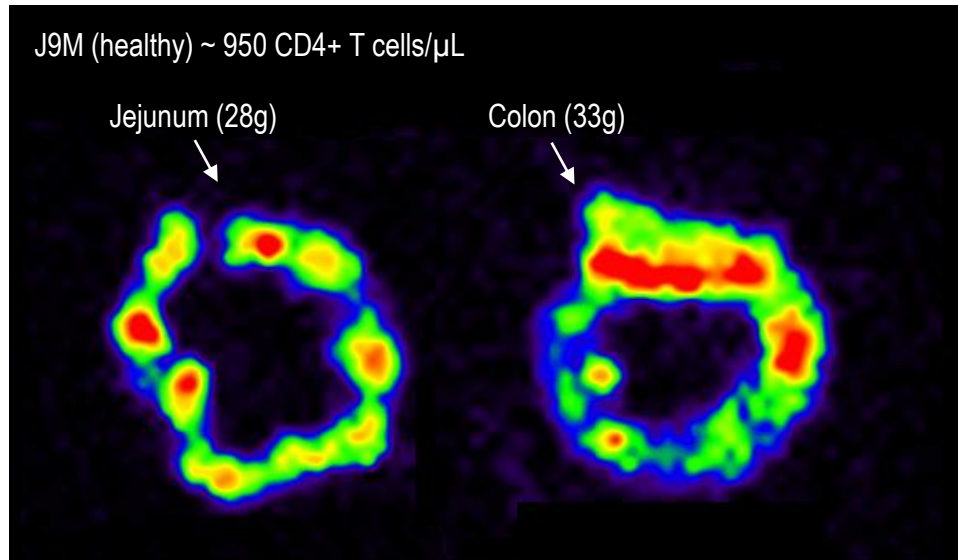**Relationship between PB CD4+ T cell counts and LT CD4 pools**
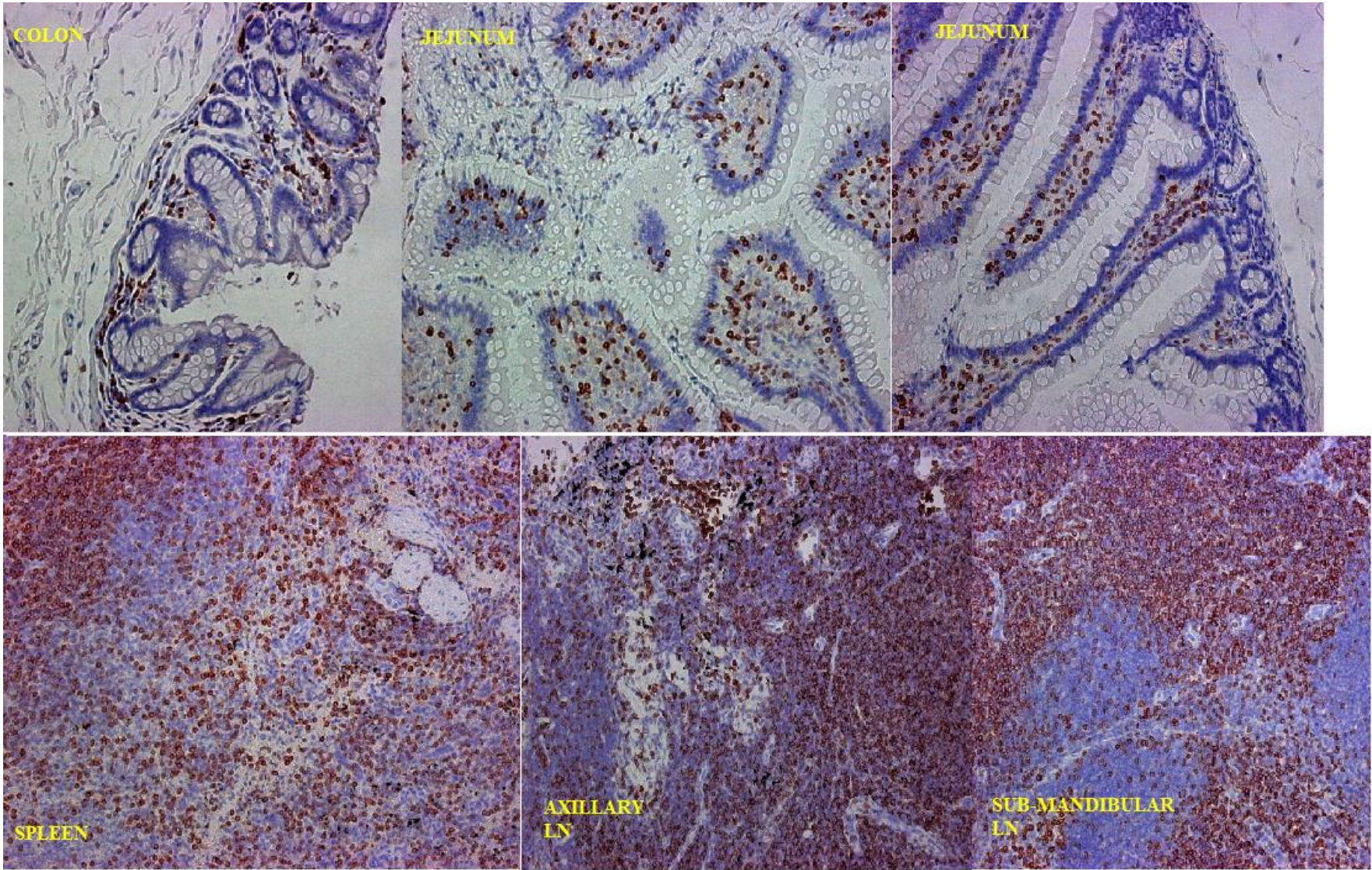
Suppl Figure S4

radio-HPLC

Baseline (pre ART)
plasma binding = > 40%

Month 1 (post ART)
plasma binding = > 40%

Month 3 (post ART)
plasma binding = > 40%

Month 5 (post ART)
plasma binding = 3.7%

Suppl Figure S5

Ex-vivo imaging

A

J9M (healthy) ~ 950 CD4+ T cells/µL

Jejunum (28g)   Colon (33g)

B

09N007 (SIVe660 infected) ~ 225 CD4+ T cells/µL
Plasma viral load = 1.25×10^6 copies/ml

Jejunum (38g)   Colon (35g)

Norm counts
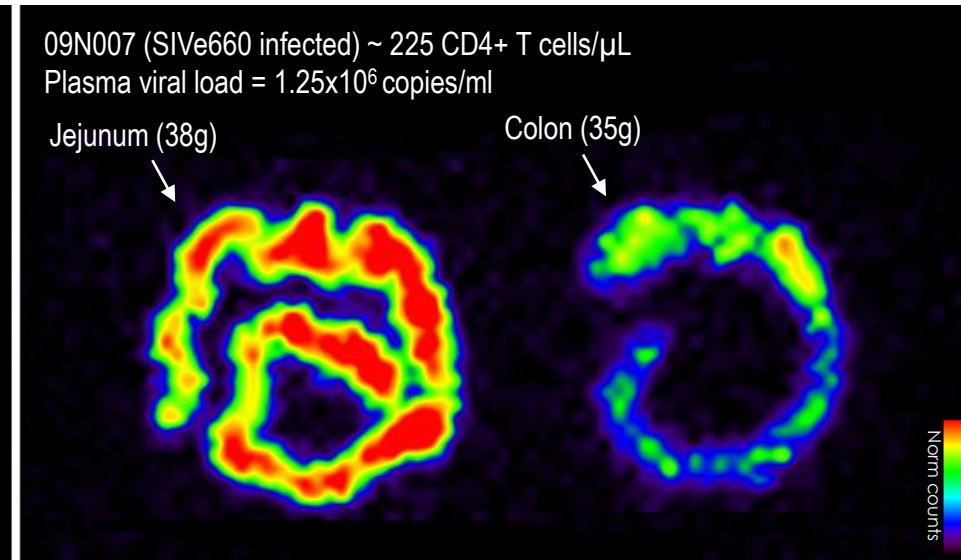
Suppl. Figure S6 A **50x**
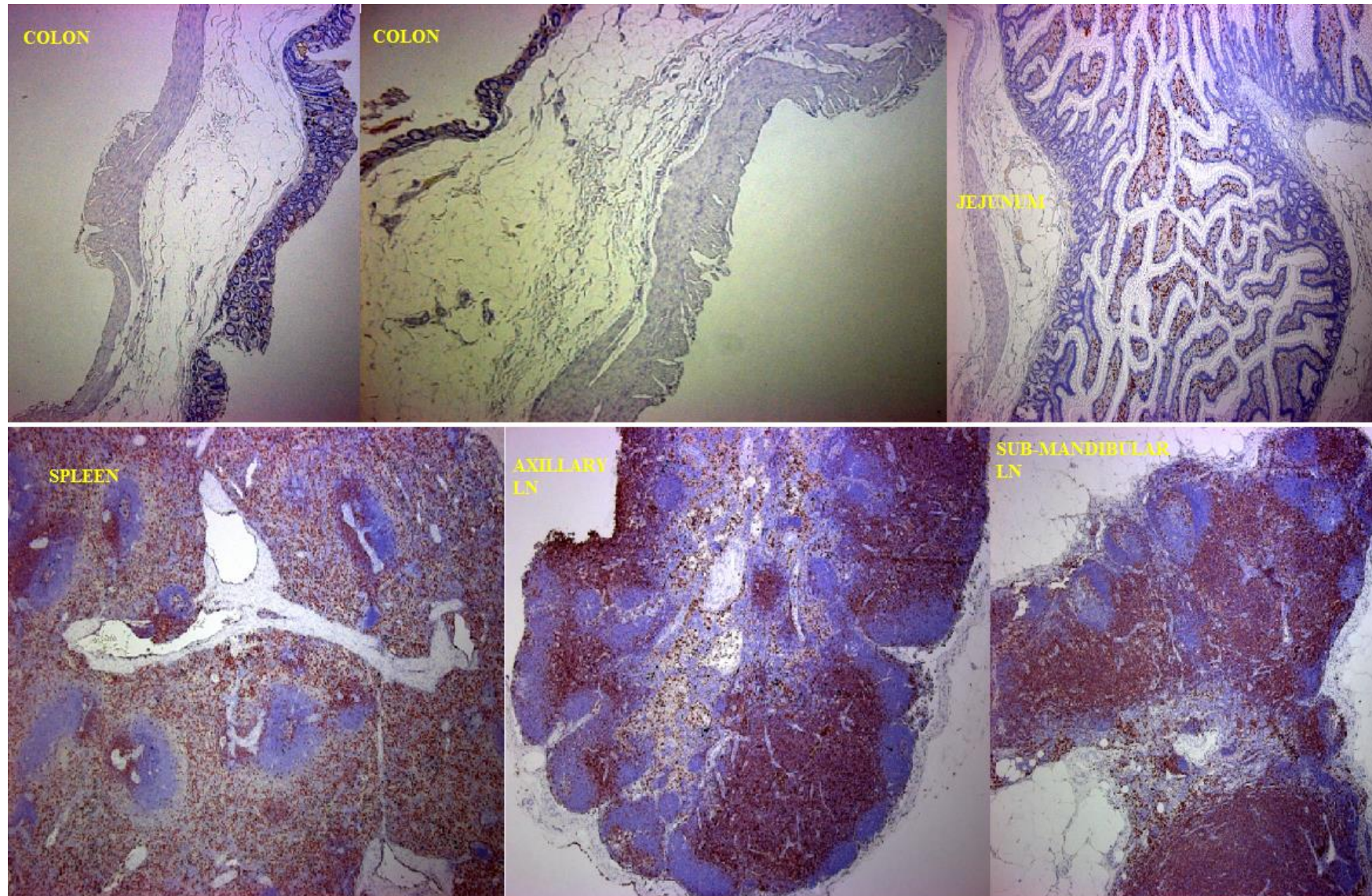
Suppl. Figure S6 B 200x

Table S3A

Animal ID	Camera	Tracer	Tc99m inj. dose (mCi)	Specific Activity (µCi/µg)
DGKG	Symbia T2, Siemens	^{99m}Tc -F(ab')$_2$-CD4R1	6.64	7.1
DG37	Symbia T2, Siemens	^{99m}Tc -F(ab')$_2$-CD4R1	5.55	5.9
MTM	Symbia T2, Siemens	^{99m}Tc -F(ab')$_2$-CD4R1	5.76	6.1
A5E006	Symbia T2, Siemens	^{99m}Tc -F(ab')$_2$-CD4R1	5.77	43.3
DBIJ	Symbia T2, Siemens	^{99m}Tc -F(ab')$_2$-CD4R1	7.85	65.5
MZC	Symbia T2, Siemens	^{99m}Tc -F(ab')$_2$-CD4R1	4.12	40.5
CE49	Symbia T2, Siemens	^{99m}Tc -F(ab')$_2$-CD4R1	7.52	78.4

Suppl. Figure S7
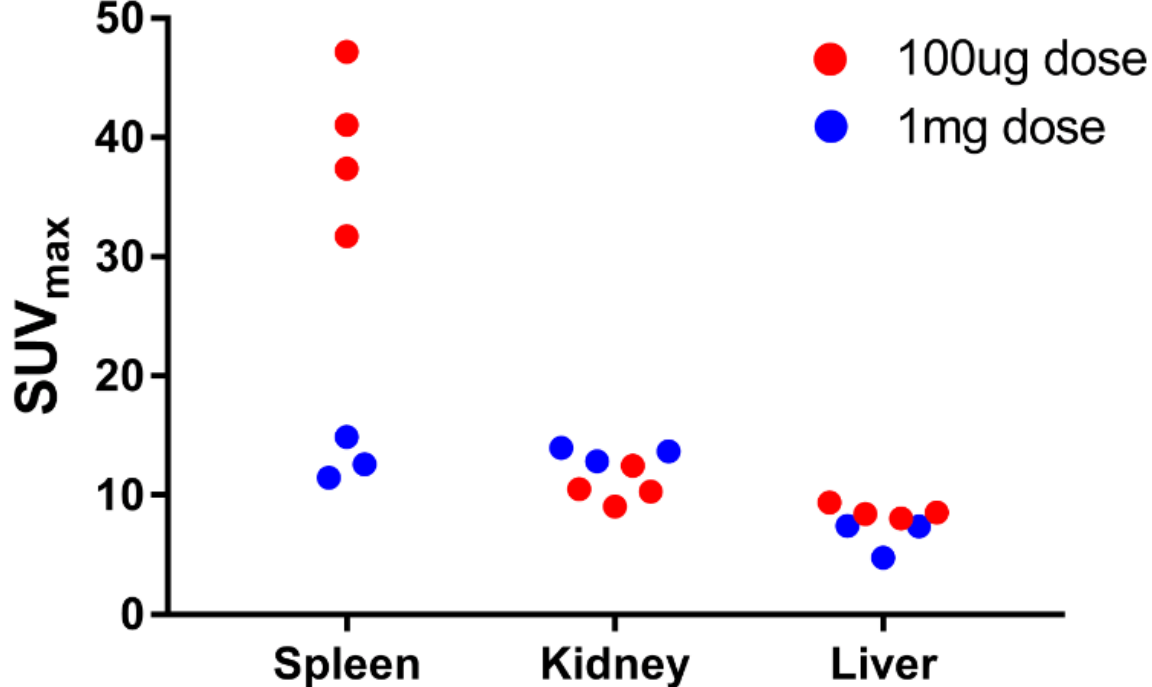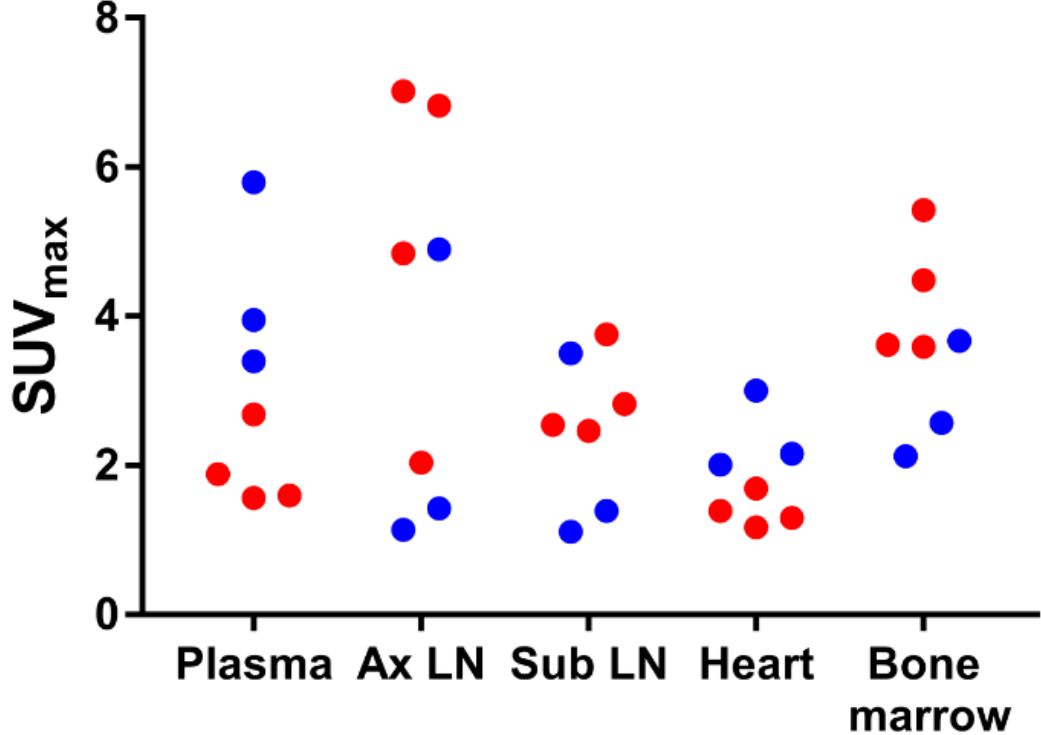
MZC (healthy) received ~100µg of CD4R1-Fab'2-^{99m}Tc
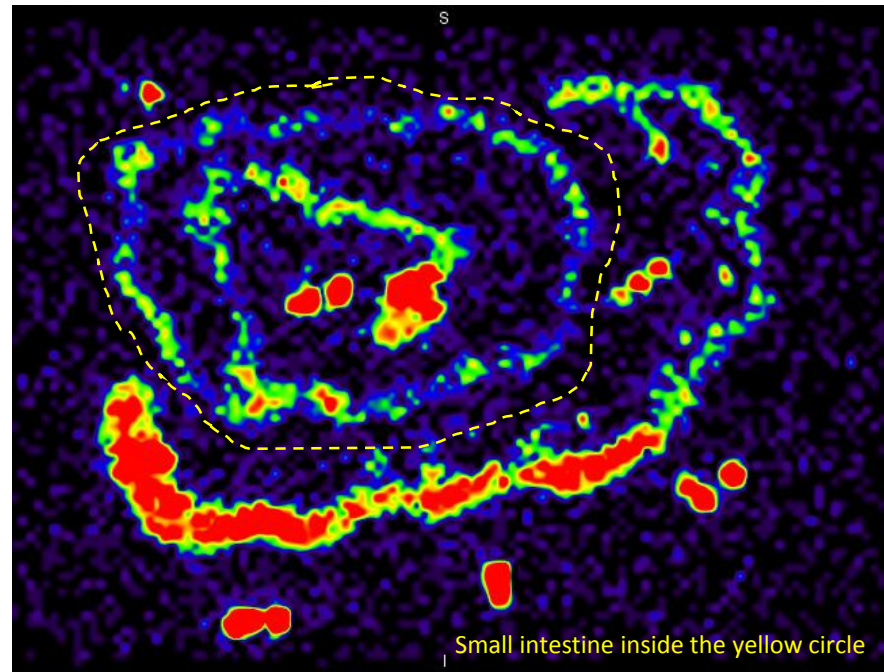
Suppl. Figure S8A

Mesenteric LN

Inguinal LN

Submandibular LN

Axillary LN

Spleen

Imaging standard

Small intestine inside the yellow circle

Large intestine inside the yellow circle

Imaging standard
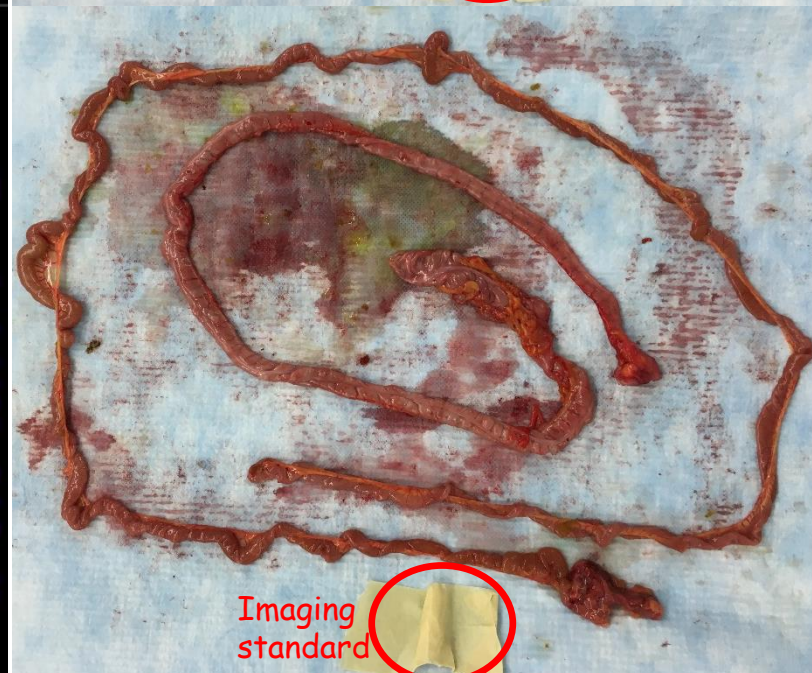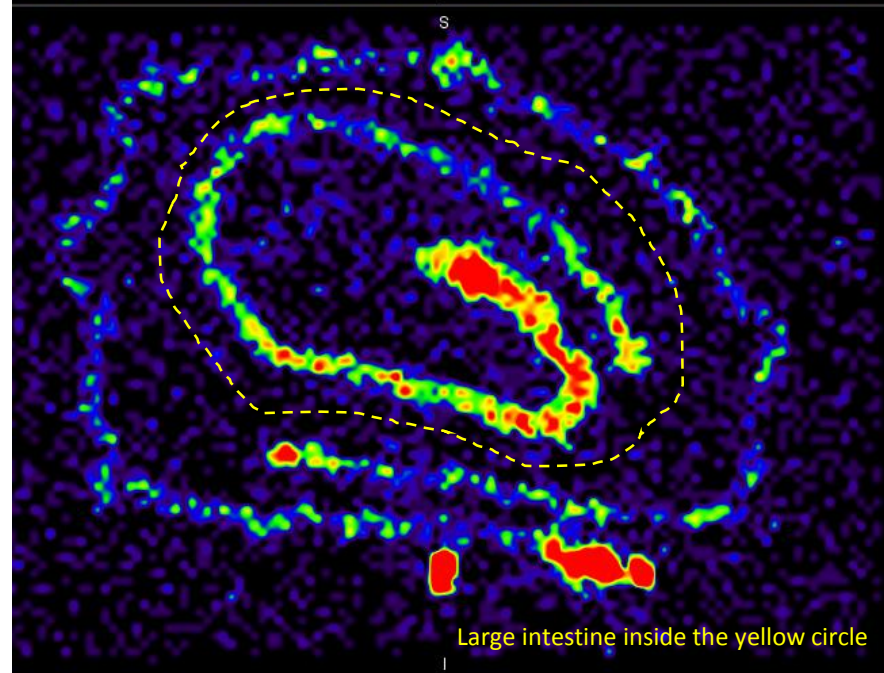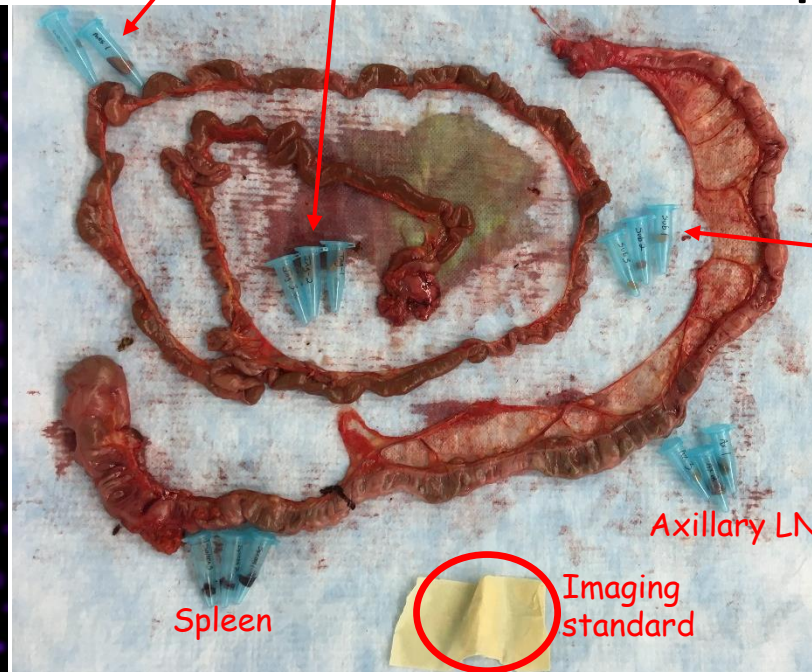
MTM (healthy) received ~1mg of CD4R1-Fab'2-^{99m}Tc

Suppl. Figure S8B
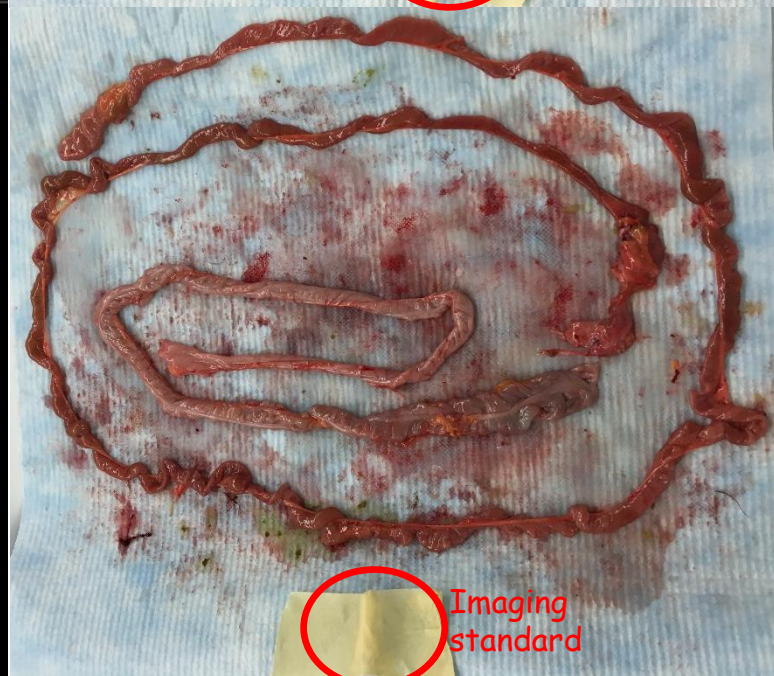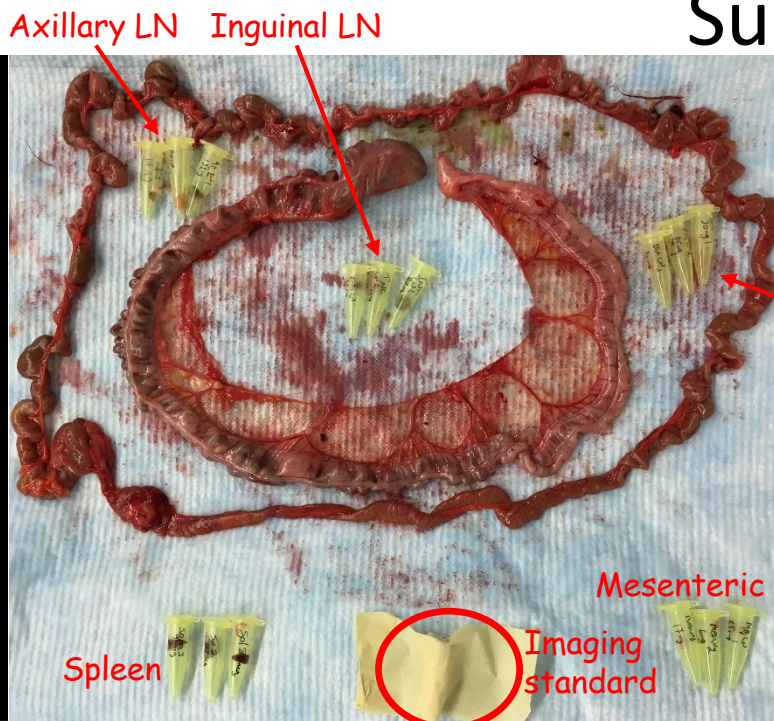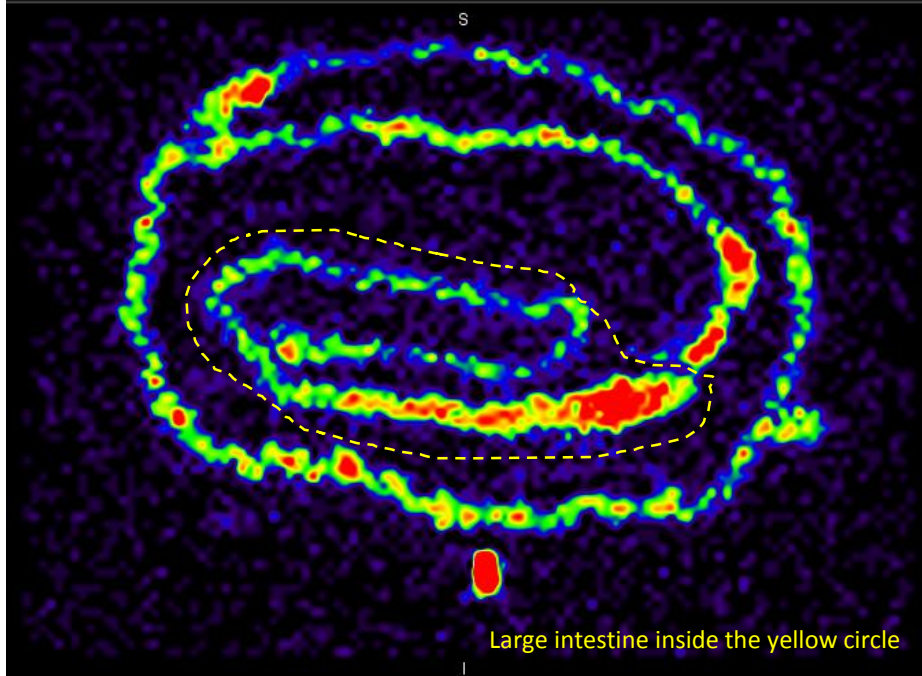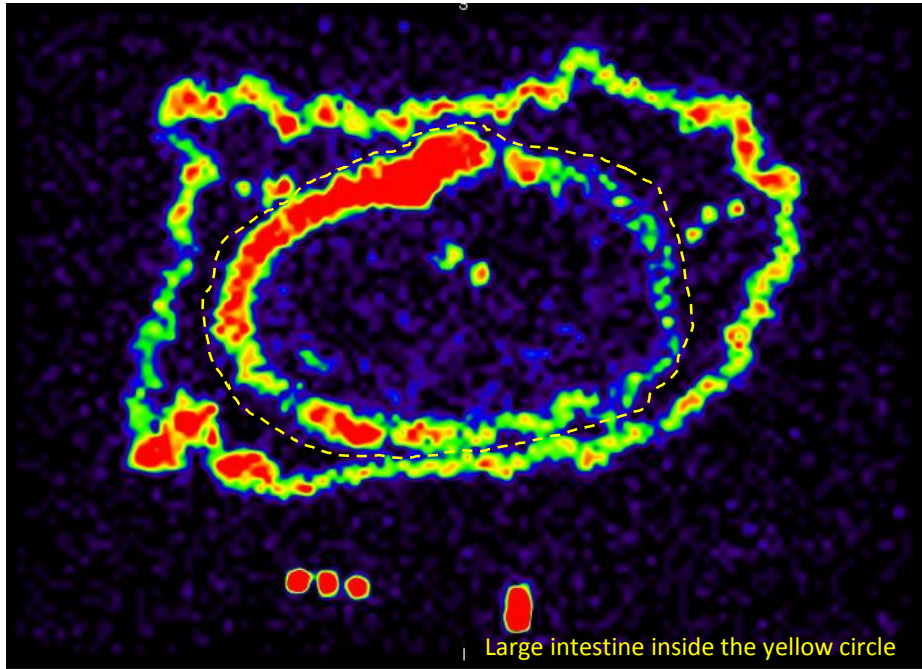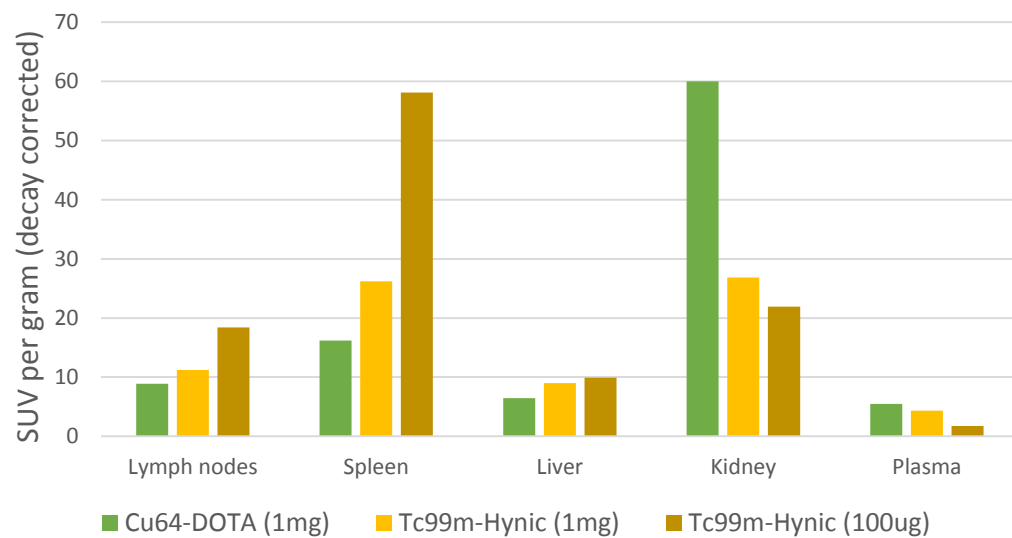
Axillary LN   Inguinal LN

Submandibular LN

Mesenteric LN

Spleen   Imaging standard

Large intestine inside the yellow circle

Large intestine inside the yellow circle

Imaging standard

Suppl. Figure S9A
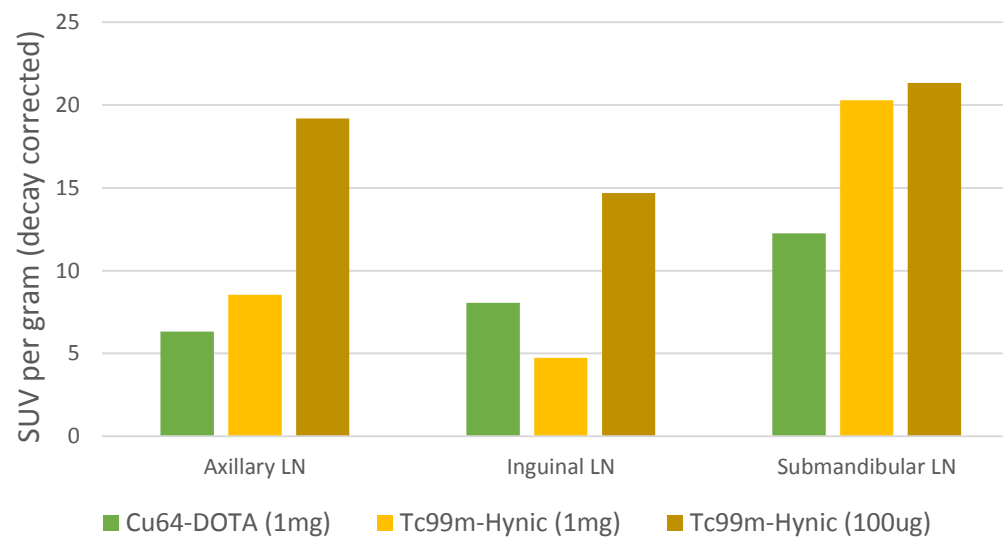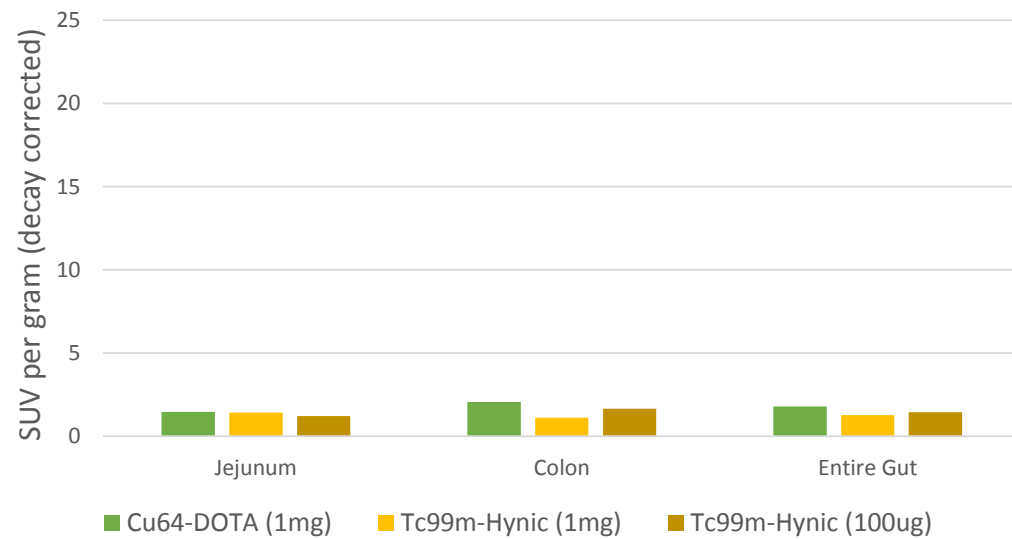
DF40 (healthy) received ~1mg of CD4R1-Fab'2-DOTA-^{64}Cu